Evolution of meniscus structures in hydrophobic granular systems

Evolution of meniscus structures in hydrophobic granular systems

Zeynep Karatza[a], Jim Buckman[b], Gabriela M. Medero[c], Christopher T. S. Beckett[a]

[a] *Institute for Infrastructure and the Environment, School of Engineering, The University of Edinburgh, EH9 3JL, UK*
[b] *Institute of Geoenergy Engineering, EGIS, Heriot-Watt University, EH14 4AS, UK*
[c] *Institute for Infrastructure and the Environment, Energy, Geoscience, Infrastructure and Society, Heriot-Watt University, EH14 4AS, UK*

Abstract

Water-repellent soils, which form naturally in arid regions or after forest fires, can be problematic for land managers and engineers as they are often associated with impeded or preferential flow paths, increased surface runoff and soil erosion. However, the reduced rainwater infiltration capacity of water-repellent soils can also result in the improvement of the stability of slopes or landfills and capillary barrier cover systems, amongst others. Understanding the hydraulic conditions within these materials is critical if issues of stability and seepage are to become tractable.

Traditional understanding of unsaturated hydrophobic soils suggests that convex water menisci, and so positive water pressures, should form between soil particles. However, the limited experimental results presented in the literature do not support this theory. In this work, the effect of particle shape on the formation and evolution of water meniscus structures is investigated at the macro (multiple particles) and particle scales, contrasting meniscus behaviours between spherical glass beads and angular sand grains.

The spreading of a sessile drop in the macro-scale is examined and found that the angularity of the sand grains has a significant effect on the apparent contact angle of a sessile drop when deposited on a mono-layer of particles. At the particle scale, Environmental Scanning Electron Microscopy was used to investigate the formation and evolution of capillary bridges and the water retention hysteresis during two wetting and drying cycles. Again, it is shown that the shape and surface roughness of the particles are controlling factors in both the formation and evolution of liquid bridges and that stable convex and concave menisci can co-exist simultaneously between hydrophobic particle surfaces. Additionally, it was found that the hydrophobic nature of the particles allowed menisci to form across much larger separation distances than could be achieved through film coalescence between hydrophilic surfaces, with possible consequences for infiltration and imbibition modelling and, more broadly, manufacturing processes relying on hydrophobic substrates. Lastly, the hydrophobic soils qualitatively exhibited overall much less hysteresis of the water retention curve than their hydrophilic counterparts.

Keywords: hydrophobic sand and glass beads, capillary bridges, hysteresis, ESEM, contact angle, goniometer

---

1. Introduction and theoretical background

Hydrophobic soils form naturally in arid regions when particles are coated with plant-derived hydrophobic organic matter compounds [48, 47] or if exposed to very high temperatures, for example during forest fires [17, 19]. Soils can also become hydrophobic if treated with contaminated water [67]

or chemicals in the laboratory [56]. Such soils can be problematic as they are often associated with reduction of soil infiltration capacity and preferential flow and may lead to increased surface runoff and soil erosion [9, 19, 63, 1]. However, the reduced rainwater infiltration capacity of hydrophobic soils can also result in the improvement of the stability of slopes or landfills and other man-made earthen structures [33, 43]. It has also been suggested that artificially induced water repellence in sands is a cost-effective alternative for capillary barrier cover systems [72, 56]. However, given their modified interaction with water, the hydro-mechanical response of these materials [e.g. 75] must be studied by engineers if they are to be used safely in geotechnical structures.

1.1. Contact angles in idealised and natural granular media

The surface tension of the interface of a solid with its surrounding air determines whether a liquid will completely spread on the surface of the solid or not. Organic coatings can decrease the surface tension of a surface, reducing its wettability [49, in our study the word "surface" refers to granular particles]. The liquid-solid-air boundary is known as the *triple line*, and the angle that forms between the liquid and the solid as the *contact angle*, θ, as shown in Figure 1. The contact angle governs soil water retention characteristics and capillary imbibition in partially saturated soils [42, 15, 33]. Specifically, the matric potential is attributed to capillary forces acting between liquid, gas and solid phases [68] and so is affected by the degree of wettability through the intrinsic contact angle [38, i.e. that dictated by surface chemistry only]. The apparent contact angle governs infiltration through packed grains and is affected by the material porosity and roughness, as well as the intrinsic

contact angle of the solid surfaces [8].

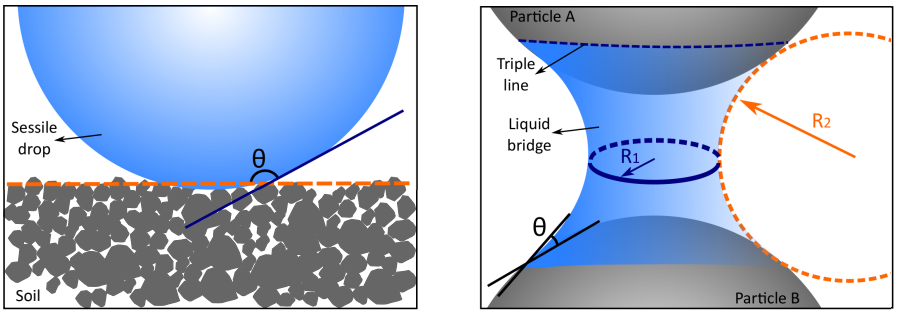

(a) (b)

Figure 1: Schematic of (a) sessile drop deposited on the surface of a hydrophobic soil and (b) a liquid bridge forming between two spherical hydrophilic smooth particles A and B

In the majority of disciplines that deal with hydrophobic and hydrophilic materials (e.g. physics, chemistry, chemical engineering), surfaces are classified as either *totally wetting* when the liquid spreads completely onto the surface (0° contact angle) or *partially wetting* (non-zero contact angle). The distinction between *mostly wetting* (i.e. hydrophilic) and *mostly non-wetting* (i.e. hydrophobic) surfaces is based on a 90° contact angle threshold [26, 69]. However, in disciplines that study soils (e.g. geology, geotechnical engineering), a soil is characterised as *non-wetting* when the contact angle exceeds 90° [5] and *wetting* when the contact angles are below 90°, with the additional assumption that a hydrophilic material must display concave menisci (i.e., by application of the Laplace equation for concave capillary bridges [11], a net attraction between particles) and a hydrophobic convex menisci (i.e. a net repulsion, by assumption of the reverse of the wetting case). There are also examples of soils being considered to be hydrophobic for apparent contact angles less than 90° [e.g. 37, 18, 72]. Here, we adopt the general definition

of "hydrophobicity", being a material with an apparent contact angle >90° but without the accompanying assumption of repulsion.

1.2. The effect of surface roughness on the apparent contact angle

Contact angles are influenced by microscopic heterogeneities of the solid-liquid interface (impurities or roughness), which cause structural rearrangements in the triple line [5, 2, 66]. For perfectly clean, smooth and flat surfaces, when the volume of a liquid increases the triple line spreads indefinitely and the contact angle remains constant (if gravitational effects are ignored). However, in the presence of surface roughness, when the volume of the liquid increases, the triple line remains stationary ("pinned") as the asperities or heterogeneities impose an additional energy barrier. The contact angle therefore gradually increases to accommodate the increasing droplet volume. When the angle reaches a certain value corresponding to the *advancing* contact angle, the tension imbalance is able to overcome the energy barrier and the triple line is mobilised. The opposite occurs when the volume of the liquid is decreased; in the presence of roughness or heterogeneities, the contact angle must reduce beyond the 'clean' value before the triple line can contract. This reduced contact angle is therefore called the *receding* contact angle. The difference between the advancing and receding contact angles is the *contact angle hysteresis [25, 22].* The pinning mechanism described here is also exhibited when the triple line meets an interface of two different solids/minerals or a sharp edge [31].

Two basic wetting models exist to describe the effect of a textured (physically or chemically) surface on the contact angle. For a physically textured surface, assuming that the roughness can be determined by a variable r

(where $r = 1$ for smooth and $r > 1$ for rough surfaces), Wenzel's model [71, 30, 51] relates the apparent contact angle on a rough surface, θ^W, to that on a smooth surface, θ^s, of the same surface chemistry, as follows:

$$\cos\theta^W = r\cos\theta^s \tag{1}$$

If a surface is smooth, yet chemically heterogeneous, then the Cassie-Baxter model [14, 51] describes the changes in the contact angle, according to the fractional surface areas occupied by each material f_1 and f_2 (where $f_1 + f_2 = 1$), as follows:

$$\cos\theta^{CB} = f_1\cos\theta_1^s + f_2\cos\theta_2^s \tag{2}$$

When a sessile drop is deposited on a physically textured *hydrophilic* surface, part of the liquid might impregnate the grooves, resulting in a pseudo chemically textured surface. Therefore the part of the liquid that constitutes the droplet will, in effect, rest on a composite surface comprising of fractions f_1 and $1 - f_1$ of solid and liquid respectively. Since the liquid in the grooves and the sessile drop have the same surface energy, the contact angle relating to the liquid fraction (θ_2^s) in Eq. 2 will be equal to zero and Eq. 2 will reduce to:

$$\cos\theta^{CB*} = 1 + f_1(\cos\theta_1^s - 1) \tag{3}$$

In the case of a *hydrophobic* physically textured surface, air can be trapped under the droplet creating a composite surface of air and solid. The Cassie-Baxter model can therefore be used and f_1 and $1 - f_1$ will correspond to the fractions of the solid substrate and the air trapped between the grooves,

respectively. The contact angle for the air (θ_2^s) in Eq. 2 will approach 180° and Eq. 2 will reduce to:

$$\cos\theta^{CB**} = -1 + f_1(\cos\theta_1^s + 1) \tag{4}$$

According to Eqs. 1-4, if an ideal surface (perfectly clean and smooth) is hydrophobic the contact angle will rise as the surface becomes rougher, making the surface appear *more* hydrophobic, whereas, a rough hydrophilic surface would appear to be *more* hydrophilic, due to the sign inversion for the cosine of angles either side of 90°.

1.3. Defining suction in hydrophilic and hydrophobic soils

Conventional understanding of the particle-scale holds that a drop of liquid between two mostly wetting (i.e. contact angle less than 90°) parallel planes forms an axisymmetric, concave liquid bridge to minimise surface energy (assuming that the particles are not in motion) [53, 60, 24, 57]. The pressure difference that exists between the interior of the liquid and the surrounding gas is known as the Laplace (or capillary) pressure, ΔP, defined as follows:

$$\Delta P = P_{in} - P_{out} = -(u_a - u_w) = \gamma\left(\frac{1}{R_1} + \frac{1}{R_2}\right) \tag{5}$$

where P_{in} and P_{out} are the pressures inside and outside of the liquid bridge corresponding to the pore water u_w and air u_a pressures respectively, γ is the surface tension and R_1 and R_2 are the principal radii of curvature of the capillary bridge (see Fig. 1(b)).

Negative values of u_w are termed "suction" (specifically, "matric" suction). "Total" suction comprises matric and osmotic components (assuming that gravitational effects can be ignored) and is a measure of the energy required to remove a unit volume of water from the soil skeleton to a reference system of pure, free liquid water. At a given absolute temperature, T, the vapour pressure, p, in a vapour above a liquid that has undergone a change in pressure, ΔP, relative to atmospheric pressure is given by:

$$p = p^* \exp \frac{V_{m_l} \Delta P}{RT} \tag{6}$$

where p^* is the saturated vapour pressure, V_{m_l} is the molar volume of the liquid and R is the universal gas constant ($8.314\,\mathrm{J\,mol^{-1}\,K^{-1}}$).

It is common to adapt Eq. 6 by assuming that $p/p*$ is equivalent to the relative humidity, R_h, [52, 28, 54, 20]:

$$s = -\frac{RT\rho_w}{\omega_v} \ln(R_h) \tag{7}$$

where s is the suction (or negative u_w), ρ_w is the density of water and ω_v is the mass of water vapour ($18.016\,\mathrm{g\,mol^{-1}}$).

The assumption in Eqs. 6 and 7, that $p/p*$ is equivalent to the relative humidity R_h, a value that cannot exceed unity, necessitates that $\Delta P \leq 0$ (i.e. this assumption is only appropriate for concave liquid bridges and will always present conditions as if the particles were hydrophilic). In this work, we will therefore not use the Kelvin equation to assign specific values of total suction to different states of R_h in the hydrophobic samples.

Even though according to Eq. 5 both positive and negative pore water pressure values could occur, hardly any evidence exists in the litera-

ture of positive pore water pressure measured in water retention curves [e.g. 8, 21, 15, 44]. Commonly, suction is measured in both unsaturated hydrophobised and non-hydrophobised soils, despite the theoretical difference in the shape of the capillary bridges forming between the soil particles. However, experimental imaging shows the formation of coexisting (or not) concave and convex capillary bridges in both natural soils and spherical glass beads [e.g. 45, 34], or of asymmetric menisci forming even between smooth, spherical particles [e.g. 23]. A disconnect therefore exists between the visual information regarding the form of these meniscus structures and the forms that must exist, mathematically, from measured suction values.

The aim of this work is to study the interaction of water with artificially hydrophobised samples of a natural sand and spherical glass beads. Specifically, we study a) the effect of particle shape and liquid volume on the static contact angle (macro-scale), using the sessile drop method; b) the effect of particle shape on the formation and evolution of capillary bridges (particle-scale), using micrographs from an Environmental Scanning Electron Microscope (ESEM), focusing on seeking evidence of repulsive and/or attractive forces between particles connected via a liquid bridge; and c) the values of the contact angles forming at the macro- and the particle-scale for hydrophobic and hydrophilic particles.

2. Materials and methods

2.1. Materials

As water repellence is induced by the bonding between the hydrophobising agents and the soil particle surfaces, soils with lower specific surface areas,

e.g. sands, are more strongly affected than finer soils [70]. Hence, for this study a highly uniform silica sand (coefficient of uniformity $C_u = 1.5$) with a mean diameter, D_{50}, of 96 µm and highly uniform alumino-silicate glass beads ($C_u = 1.3$) with a D_{50} of 84 µm were selected. Both spherical glass beads (i.e. regular pore space/smooth particle surface) and more angular silica sands are tested to examine the differences in the evolution of meniscus structures, given that the wettability of dry or partially saturated porous media is determined by the geometry of the pore space as well as the surface tensions of the interfaces [5]. The specific type of sand was chosen because it has been shown to react well with the hydrophobising agent, as discussed below [58], and because of previous research of Beckett et al. [12, 10] performed on the same sand, which provides a good basis for comparison.he glass beads were chosen to observe the "classically" assumed case where menisci form axisymmetric concave structures between curved hydrophilic surfaces but convex structures between the same surfaces, at similar separation distances, when hydrophobic. Both hydrophobic and hydrophilic sand and glass beads samples were tested and the following acronyms will be used throughout this paper: HPB → **H**ydro**p**ho**b**ic; HPL → **H**ydro**p**hi**l**ic; GB → **G**lass **B**eads; S → **S**and.

Figure 2 shows images of both materials and the particle size distribution curves measured by laser diffraction using a Beckman Coulter LS230 particle size analyser, which measures the grain sizes of particles in suspension in the range of 0.4 µm to 800 µm. The maximum particle size increased slightly between the hydrophilic and hydrophobic glass beads. However, as this effect was not identified in the sand, it is likely that this difference was due to

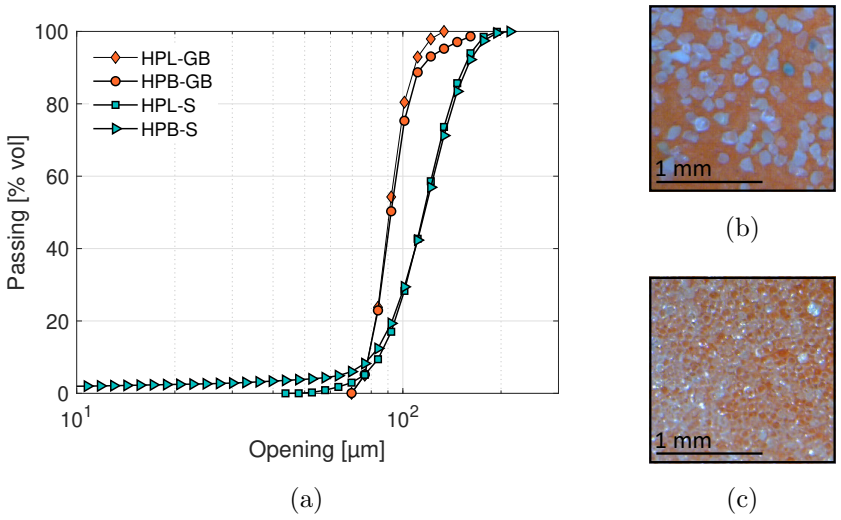

(a) (b) (c)

Figure 2: (a) Particle size distributions; (b) silica sand; (c) glass beads

the small sample size and a minor heterogeneity in the particle sizes; we do not believe that particles were adhered to each other. The hydrophobic sand appears to have a wider range of fines, however this is likely to be an accumulation of dust in the particle size analyser. It could also indicate that some particles broke during the mixing of the hydrophobising agent with the sand, resulting in an increase in the amount of fines.

The glass beads are highly spherical and the sand particles are sub-rounded of medium sphericity, according to the manufacturer. The particle size limits of both materials ($D_{\text{min}} = 63\,\mu\text{m}$ and $D_{\text{max}} = 106\,\mu\text{m}$) were chosen to ensure a good resolution during ESEM testing.

2.2. Hydrophobising agent

Several methods have been used to impart hydrophobicity to sands, for example stearic and/or oleic acids, waxes and organic silanes. Oils and waxes

have the advantage of being less hazardous to apply to soil substrates than silanes but might not be as hydrophobising [e.g. 43]. Stearic and oleic acid treatments have been used to explore the behaviour of large-scale systems, for example, in capillary barrier systems [65], the effect of particle size and uniformity of gradation on the degree of water repellence [72] and the accuracy and reproducibility of water repellence measurement techniques [41]. To study the change in the shear strength properties when a coarse soil is hydrophobised, Karim et al. [35] used organic silane to form hydrophobic films around Ottawa sand, whereas Bardet et al. [6, 7] studied wax-coated sands. Bauters et al. [8] studied the effect of water repellence on the constitutive relationships during imbibing by mixing sands with an ethanol solution containing a small amount of octadecyltrichlorosilane.

Researchers have used dimethyldichlorosilane (DMDCS) to create hydrophobic samples of sands or glass beads to observe water meniscus shapes [45, 12, 10, 43, 34]. DMDCS was therefore selected for this study to allow results to be compared to previous work [see 10]. Water repellence was induced by mixing 1 ml of DMDCS with 500 g of each granular sample to coat the particles and lower their surface energy to decrease wettability. The ratio of DMDCS to sand was based on the average particle size of each granular sample, according to Ng and Lourenço [56], following an almost identical procedure.

2.3. Measuring the contact angle in the macro-scale: the sessile drop method

The value of the apparent contact angle is strongly affected by the measuring technique [5] and several methods have been used to measure it. For example, the capillary rise method [e.g. 5] and the Wilhelmy Plate method

[e.g. 46] measure contact angles associated with advancing or receding wetting fronts (the latter method which was modified by Bachmann et al. [5] to be used for hydrophobic soils). Additionally, methods such as the water drop penetration time and the molarity of an ethanol droplet are also used to characterise water repellence and its persistence in soils [40, 74] regardless of the value of the apparent contact angle.

To measure the static apparent contact angles the sessile drop method was selected for this study as it is able to measure both hydrophilic and hydrophobic contact angles [e.g. 4, 5, 73, 35, 33]. Bachmann et al. [4] showed that, for fine to medium granular materials, the contact angles can be determined with the sessile drop method with an accuracy on the order of 6°.

To determine the static apparent contact angle a set of four drops of deionized water of 5 µl each were deposited on a horizontal mono-layer of the granular materials at different locations, as outlined by Bachmann et al. [3]. The volume of each drop was gradually increased to 80 µl by adding water in increments of ∼5 µl to each droplet to investigate the evolution of the contact angle. Immediately after the deposition/addition of each drop a 12 sec video was captured and the equilibrium apparent contact angle was measured for each frame. The test was performed using a Krüss GmbH DSA30S drop shape analyzer/goniometer. The goniometer has a camera with 1200 × 800 px at 200 fps to 90 × 60 px at 2000 fps resolution. We used the higher resolution with a frame rate of 50 fps to capture the profile of each drop; since the test was notionally static a higher frame rate would have been redundant.

The analysis was performed using a built in software for contact angle

analysis [ADVANCE, 39], using the "Ellipse (Tangent-1)" fitting method and a manual baseline detection. This fitting method assumes an elliptical drop shape, has a measuring range between 10° and 120° and is able to measure the contact angle of both axisymmetric and slightly asymmetric drop profiles. A template was created to define a single baseline for all the drops deposited on the same surface, increasing the repeatability of the process and permitting the measured contact angles to be compared more precisely. The radius of the triple line is calculated separately from the contact angle, using the coordinates of the intersection of the drop profile and the baseline.

It should be mentioned that the rough contact surface, as opposed to a smooth, clean and reflective surface that is suggested for any contact angle measurement using a goniometer, impeded the definition of the baseline. Saulick et al. [61] developed a semi-automated method using a combination of commands in an open source image processing software, Fiji [62], to fit the contour of the sessile drop and identify a precise baseline.It should be mentioned, however, that their method requires a larger number of user defined steps (e.g. binarisation of images, placement of baseline, identification of points along the drop profile) in comparison to the approach used in this work. McCerery et al. [50]have used the open source program PyDSA to detect the baseline and the drop profile and fit an ellipse to determine the contact angle. This algorithm, however, uses the reflection of the sessile drop to determine both the placement of the baseline and subsequently the tangent to the drop profile and might therefore not be appropriate for the case where the sessile drop is deposited on a granular, non-reflective surface. We, therefore, believe that improved consistency between measured profiles

could be achieved by using ADVANCE for the fitting of the drop profile when creating a template for the definition of the baseline.

2.4. Observing liquid bridge formation and evolution

A dry sample of each granular material was placed on the ESEM stage [QUANTA FEG 650; see 16, for details], whilst the partial pressure of water vapour in the specimen chamber was controlled to investigate the formation and/or regression and shape of the liquid bridges. Initially, a single layer of particles was placed on a flat surface onto which a microscopy stub with a double sided tape was pressed for 10 sec. When a layer of the particles was adhered onto the stub it was placed into the peltier stage of the ESEM. This preparation method resulted in regions of looser and denser packing, allowing the effects of different separation distances to be observed at different points within a single specimen. To achieve a relative humidity of 100 % for the operating range of the scanner, the temperature of the specimen chamber was reduced to and kept constant at 5 °C.

Each investigation cycle comprised a wetting stage followed by a drying stage. The wetting stage started from an initial R_h equivalent to 61.3 %, gradually increasing to 100 % respectively at a constant rate of $0.027\,\mathrm{kPa\,min^{-1}}$, whilst decreasing at the same rate to the initial value of R_h (i.e. drying stage) completed a cycle. The cycle was repeated leaving the sample to stabilise for an additional 2 min at the end of each wetting or drying stage (the sufficiency of this time was confirmed visually). The hysteretic effect of the water retention response of unsaturated soils (i.e. difference between wetting and drying response) is expected to be less prominent in the second drying and onward [55, 36], which is why each cycle was repeated.

3. Results and discussion

3.1. Evolution of the apparent contact angle

Figure 3 shows the evolution of the sessile drop contact angle with increasing droplet volume for the hydrophilic (Fig. 3(a)) and the hydrophobic (Fig. 3(b)) sand and glass beads. A second order polynomial regression was fitted to the data in Figure 3 to accentuate differences in the behaviour of the glass beads and the silica sand; results of contact angles higher than 120° (circled in Fig. 3(b)) were omitted from the fit as they lie above the limit that the goniometer's fitting method can measure accurately. Notably, contact angles for the sand appeared to increase with increasing droplet volume towards a steady-state value, whereas contact angles for the glass beads were nominally constant, within the scatter of the data.

Given that spheres possess the lowest solid fraction in a random close packing state [13] and that increasing polydispersity in a sample permits packings of higher solid fraction, the angularity of the sand particles and their slightly less uniform grading compared to that of the glass beads means that the surface of a mono-layer of sand particles will be slightly smoother than that of the glass beads. Hence, according to the wetting models described in Sec. 1.2, the contact angles for HPL-S and HPB-S are higher and lower, respectively, than their glass bead counterparts, as shown in Fig. 3. This does not, however, explain the increase in contact angle observed for the sand particles in both the HPB and HPL states.

A factor when examining the shape of droplets of increasing volume is the transgression of the capillary length. When the volume of a drop increases to the point where gravity is no longer negligible, the drop starts to flatten (i.e.

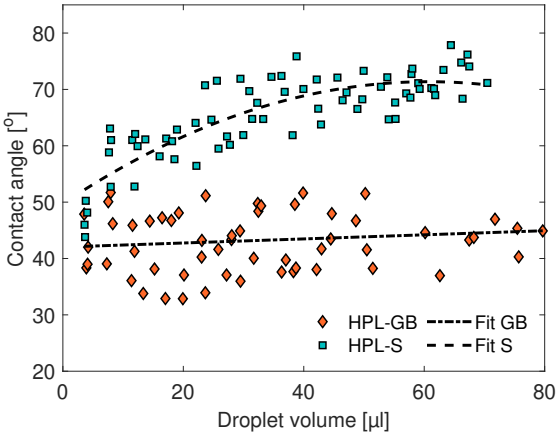

(a) Fit GB: y = $3.2429e^{-6}$x^2 + 0.036x + 42.0298 – R^2 = 0.0196
Fit S: y = -0.0059x^2 + 0.7135x + 49.7154 – R^2 = 0.7

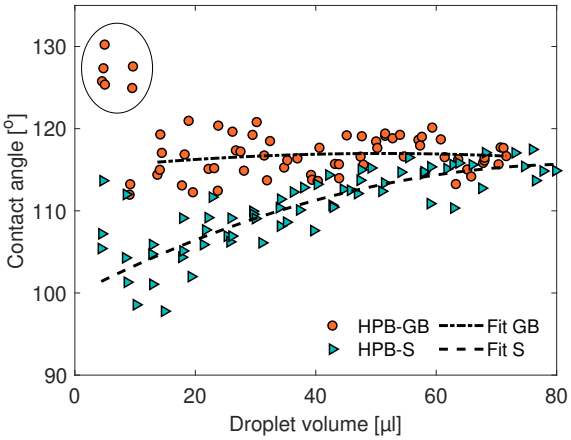

(b) Fit GB: y = -0.0008x^2 + 0.0773x + 115.0053 – R^2 = 0.0189
Fit S: y = -0.0022x^2 + 0.3765x + 99.7942 – R^2 = 0.7615

Figure 3: Evolution of the static apparent contact angle on (a) hydrophilic surfaces and (b) hydrophobic surfaces

heavy drops); the droplet radius above which gravity begins to dominate is given by the capillary length, κ^{-1}:

$$\kappa^{-1} = \sqrt{\frac{\gamma}{\rho g}} \tag{8}$$

For an air temperature of 20 °C, water has a density, ρ, of 998.23 kg m^{-3} and a surface tension, γ, equal to 72 mN m^{-1}, giving a capillary length of 2.71 mm. The droplet volume, V, corresponding to the capillary length for a given contact angle, θ, can be calculated via:

$$V = \frac{\pi}{3}\left(\kappa^{-1}\right)^3 (2 + \cos\theta)(1 - \cos\theta)^2 \tag{9}$$

where it is assumed that the droplet is a spherical cap of a uniform radius of curvature. For those contact angles shown in Figure 3, the equivalent droplet volumes at the capillary length lie at 4.12 µl for the HPL-GB and between 7.03 and 21.3 µl for the HPL-S, and between 49.3 and 66.5 µl for the HPB-S (the upper limit is the same for the HPB-GB), i.e. some flattening would have occurred, particularly in the majority of measurements made on the hydrophilic soil substrates. Theoretically, however, the flattening should not have affected the values of the measured contact angles [27].

Figure 4 shows the measured triple line radii versus droplet volume, compared to the theoretical triple line radius for a hemispherical droplet (i.e. a droplet with a contact angle of 90°, where the triple line and droplet radii are equal). The glass beads and sand results show little deviation from the expected cubic relationship between triple line radius and droplet volume either above or below the capillary length, suggesting that droplet flattening was negligible (a flatter droplet would have a faster increase in triple line radius than a more spherical droplet). Note that the largely hydrophilic glass beads together with the lower solid fraction they possess, allowed the liquid

to penetrate the granular base distorting the circular shape of the triple line, leading to the slight deviations of HPL-GB shown in Figure 4. Therefore, droplet flattening was indeed not a significant contributing factor and, alone, cannot explain the changes in contact angle found for HPL and HPB sand seen in Figure 3. Good agreement with the cubic relationship also provides confidence that the selection of the droplet baseline using ADVANCE was successful.

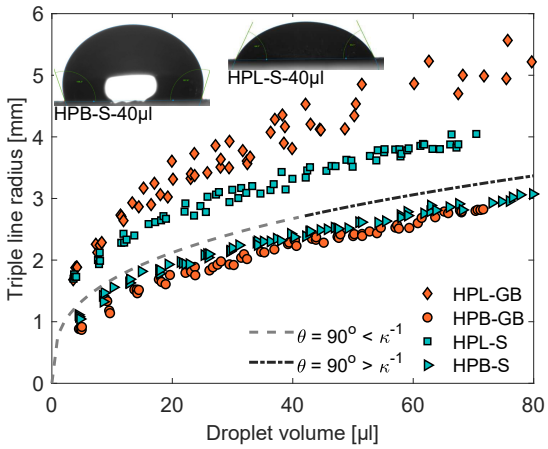

Figure 4: Evolution of the triple line radius of a sessile drop deposited on both hydrophilic and hydrophobic surfaces [Inset images: example droplets of the same volume on hydrophobic and hydrophilic surfaces (not to scale)]

Additional factors affecting the contact angle of a droplet are the surface roughness and chemical heterogeneity, as explained in the opening sections. The definition of a textured surface is independent of the volume of the deposited droplet, therefore, it may be assumed that the roughness/chemical heterogeneity (i.e. r and/or f_1) remain constant. Even with ignoring this assumption, changes in roughness cannot explain the increases in contact

angle for both HPL-S and HPB-S with increasing droplet volume; a change in roughness would have the *opposite* effect on HPL-S as for HPB-S, again as discussed previously.

Although the sand may present a smoother surface to the droplet than the glass beads, the sand surface will comprise distinct exterior corners, whereas the glass beads present a (nominally) uniform curvature. It is well understood that the advancing contact angle becomes pinned at a sharp edge and must increase to a critical angle to navigate the change in geometry [e.g. 59]. A steady increase in contact angle may, therefore, indicate an increasing contribution of edge effects to the overall contact angle. A simple model was created to explore this potential effect, wherein it was assumed that:

- the triple line is constantly circular;
- the bed of particles can be approximated as a two-dimensional grid of equilateral triangles of arbitrary height = 1 and edge length a, where the edges of each triangle correspond to the edge of a particle;
- the triple line can be pinned only when it intersects the edge of a shape;
- edges within the triple line have no effect on the value of the contact angle [for details about this assumption see 51];
- a perpendicular intersection between the triple line and a particle edge has no effect on the triple line contact angle, whereas a tangential intersection has the greatest effect;
- contact angles can be described by a face contact angle, θ_F, (i.e. unpinned, where the triple line is not in contact with the edge of the

particle) and an edge contact angle, θ_E (i.e. pinned), where $\theta_E \geq \theta_F$;

- a tangential intersection has a greater effect on the contact angle as the droplet radius increases, due to the increased length of triple line in proximity to a straight edge; and

- the overall droplet contact angle for a triple line of a specific radius is the weighted mean of the length of the triple line that is affected by edges and that which is not.

A triangular grid was chosen to capture, in some way, the angularity of the sand particles as shown in later micrographs. A simple function of $\sin\beta$ was used to weigh the effect of intersection angle, β, on the triple line contact angle, where $0 \leq \beta \leq 90^\circ$ and where $\beta = 0^\circ$ is a perpendicular intersection and $\beta = 90^\circ$ is tangential (see Fig. A.1 in appendix for more details). Where the triple line intersected a node (the junction of multiple triangles), the highest value of β was used. It was assumed that a triple line of a small radius, r, would deflect away from an edge more rapidly than one of a larger radius; therefore, a weighting of $\cos\phi$ (where ϕ is the arc angle as defined in the appendix) was used to weigh the effect of the size of the triple line radius on the edge contribution. The overall length of the triple line affected by a *single* edge was therefore given by $w = a\ \sin\beta\cos\left(\tan^{-1}\left(\frac{a}{r}\right)\right)$, and the final value of the contact angle given by:

$$\theta = \frac{1}{2\pi r}\left[\theta_E \sum_{i=1}^{n} w_i + \theta_F\left(2\pi r - \sum_{i=1}^{n} w_i\right)\right] \tag{10}$$

where n is the number of edge intersections, and the percentage influence of the edges on the final contact angle is $100\frac{\sum_i w_i}{2\pi r}$. The calculation stages are

399 provided in more detail in the appendix to this article.

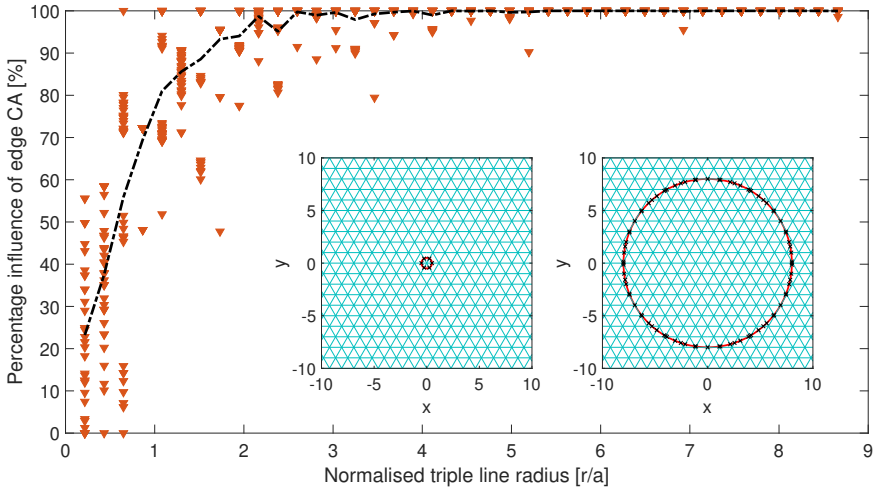

Figure 5: Evolution of the contribution of edges to the overall contact angle (average shown in dashed black) [Inset: example intersections (black crosses) for triple lines (red) of arbitrary radii of 0.5 (left) and 8 (right; triple line centred at (0,0) for both)]

400 The results of the model described above are shown in Figure 5, where
401 individual results were calculated for triple lines of arbitrary radii between
402 0.25 and 10 and for central eccentricities from the origin between 0 and
403 0.5 in the x and y directions (to avoid periodic results due to the simple
404 geometries used). Figure 5 is presented in terms of percentage contribution
405 of edges, rather than contact angle, as the values chosen for θ_E and θ_F are
406 arbitrary in this approach. For small triple line radii, the contribution of
407 edges to the contact angle is small and the overall contact angle is close
408 to θ_F, as few intersections exist. As the triple line radius increases, the
409 number of intersections, and the number of those that are more preferentially
410 orientated, increases, so that the contribution of edges to the overall contact

angle also increases and approaches θ_E. As this mechanism does not require an assumption about the values of θ_E and θ_F, save only that $\theta_E \geq \theta_F$, an increase in contact angle would be expected with increasing triple line radius, and so droplet volume, for both hydrophilic *and* hydrophobic surfaces.

That this model is crude is not in doubt and to draw quantitative conclusions from Figure 5 would be inappropriate. However, the qualitative match to Figure 3 suggests that edge effects, which were not present in the glass beads, were responsible for the increases in contact angles observed for the sand surfaces.

3.2. Liquid bridge formation and evolution

The ESEM micrographs (resolution of 0.19 µm/px) were analysed using Fiji, an open source image processing software [62], to study the wetting and drying response of the granular materials. In the following we investigate the *pendular* regime where a capillary bridge is associated with exactly two particles, the *funicular* regime with liquid clusters that are simultaneously in contact with three or more particles, and finally the *capillary* regime where the assembly is fully saturated.

Two tests per material were carried out (denoted as -01 and -02 respectively) to investigate the effect of packing and therefore separation distance in the formation and loss of capillary bridges. -01 tests examined 'denser' packing than -02 tests (noting that, for a mono-layer of particles examined at the particle scale, the idea of density is misleading). For brevity, images will be presented mainly for the denser samples (-01), which allowed for the development of more liquid bridges due to the smaller separation distances between the particles.

3.2.1. Glass beads

Table 1: Glass beads' sample properties as measured from the ESEM micrographs (the separation distances shown below are measured for particles connected via a liquid bridge)

Sample	Solid [%]	Average Separation Distance [µm]	Min Separation Distance [µm]	Max Separation Distance [µm]
HPL-GB-01	78.4	0.5	0.0	1.3
HPL-GB-02	72.0	0.94	0.4	1.4
HPB-GB-01	72.5	3.3	0.1	17.7
HPB-GB-02	67.5	4.8	0.0	13.6

Table 1 shows the differences between the percentage of solid occupying the images (i.e. an indication of 'density'), as well as the separation distances at which liquid bridges formed during the pendular regime. To get an equivalent of a solid fraction, the initial images were segmented into the solid phase and its surrounding space. Then the ratio of solid voxels to the whole image size was computed to identify the space occupied by solid (Table 1). After individual particles were identified, an ellipse was fitted to detect the centroids of each particle, from which the separation distances were calculated. On average, liquid bridges at slightly larger separation distances formed in the looser samples. Notably, in the hydrophobic soils menisci formed on average at 4-6 times larger separation distances, with examples of liquid bridges

forming at distances of almost 20 µm (∼1/4 of the particles' D_{50}).

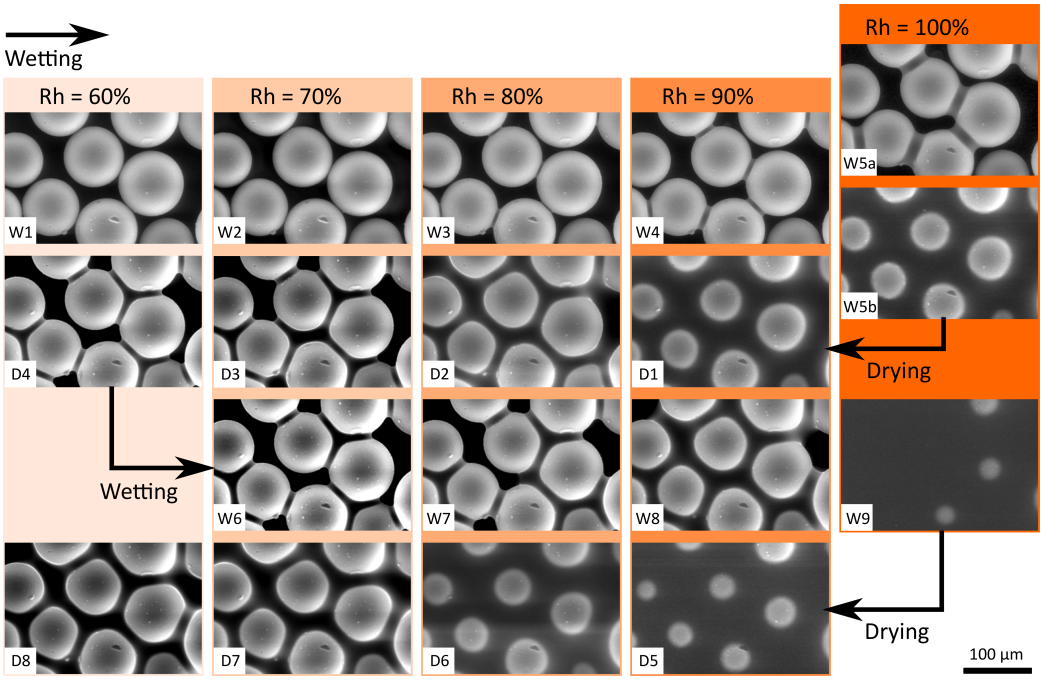

Figure 6: ESEM micrographs showing particles undergoing two wetting and drying cycles for HPL-GB-01

Figure 6 shows the evolution of menisci structures in HPL-GB-01. Each column presents images at the same R_h and each row corresponds to one stage (wetting or drying); the same style is adopted for HPB-GB-01, HPL-S-01 and HPB-S-01 results.

In the initial wetting, concave liquid bridges form between particles with the smallest separation distance (Fig. 6-W3). New menisci form as R_h increases and the volume of previously formed bridges increased accompanied by the spreading of the triple line, resulting in an advancing contact angle of approximately 20 to 25° (measured using Fiji, by fitting an ellipse around the particle and one on the outer curve of the concave liquid bridge and mea-

suring the angle between them). There is some evidence of particles moving closer when a new bridge forms between them indicating suction, however the motion was only at the pixel level and not discernible in a still image (see the online version of this paper for a video submission, showing this movement). Until the end of the initial wetting phase the sample is consistently in the pendular regime, before suddenly flooding (reaching a capillary regime) when the chamber reaches $R_h = 100\,\%$ (Fig. 6-W5a $\rightarrow$ W5b).

During the first drying phase the water gradually evaporates and a network of interconnected bridges forms reaching a funicular regime that is not evident during the initial wetting phase (Fig. 6-D3). With a further reduction in R_h, in cases where the separation distances are smaller than the average distance at which a single bridge formed initially, the bridges separate from the network forming menisci between two particles, whereas when the separation distances are large ($> 1.5\,\mu m$) they rupture and the water redistributes to the remaining menisci, presumably travelling via nanoscopic films adsorbed onto the particle surfaces (Fig. 6-D4).

Similarly to the initial wetting phase, the receding contact angle remains relatively constant at values of approximately 20 to 25°, indicating very little, if any, contact angle hysteresis and thus confirming the relatively smooth surface of the glass beads. Some particles were observed to move apart once a bridge ruptured, due to being attracted by remaining bridges with other neighbouring particles; again, movements were on the pixel scale but are visible in this paper's accompanying video submission. The sample reaches a capillary regime faster during the second wetting phase (Fig. 6-W9) and the saturation ratio only slightly decreases during the second drying stage,

exposing only the tops of the particles and constantly remaining in a capillary regime (Fig. 6-D8).

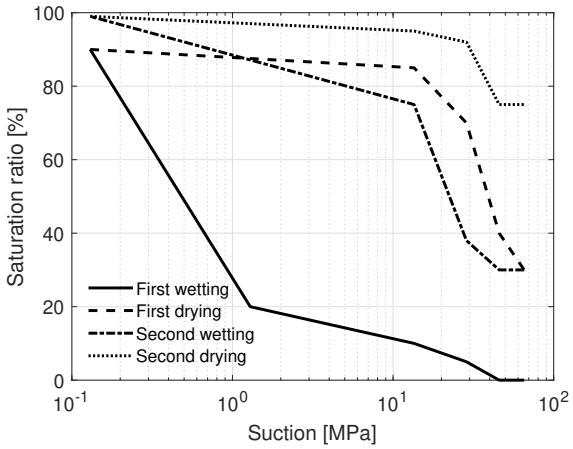

Figure 7: Schematic of the retention curve for the wetting and drying phases of the hydrophilic glass beads

presented in Fig. 6

Comparing Figures 6-W7 and D6 indicates significant hysteresis in the retention characteristics of the assembly. This hysteresis is shown schematically in Figure 7, where the degree of saturation has been measured from the percentage of water occupying the micrographs and the values of suction have been calculated using Eq. 7, given that all of the observed menisci are concave. The image was binarised into two phases (i.e. water and surrounding space), and from the voxels corresponding to the water, and solid found earlier, the saturation ratio was calculated. We note, however, that it is not possible to measure an actual retention curve for this material using this approach, as the ESEM sample is a mono-layer, so that the engineering significance of the behaviour presented in Figure 7 cannot be determined.

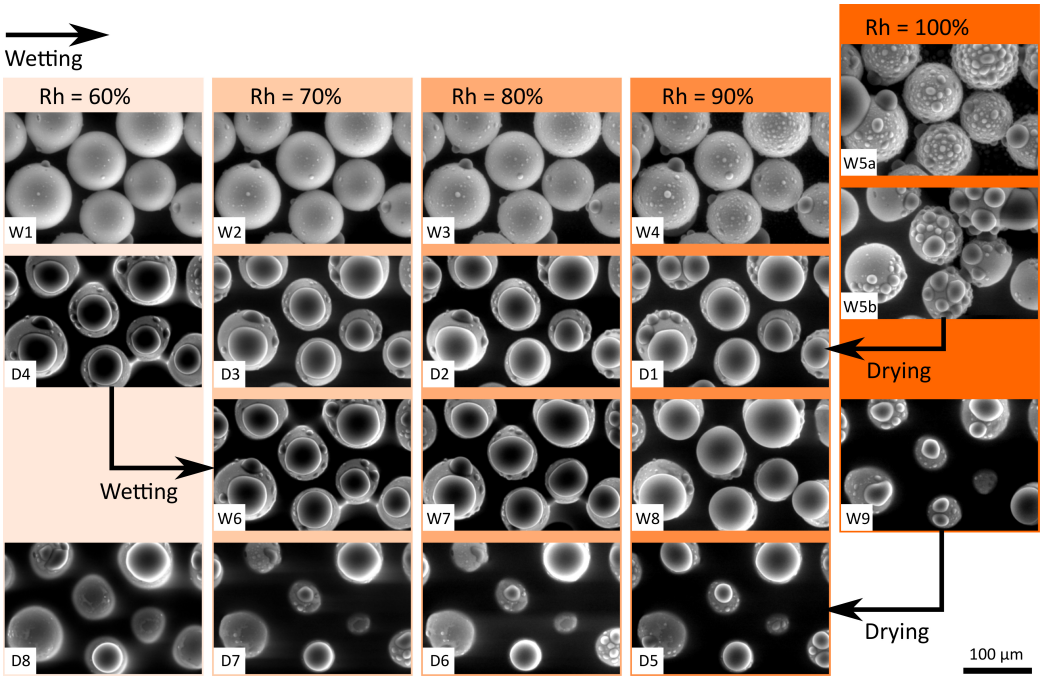

Figure 8: ESEM micrographs showing particles undergoing two full wetting and drying cycles of HPB-GB-01

Figure 8 shows the evolution of droplet and meniscus structures in HPB-GB-01. Due to the hydrophobic nature of the particles, condensation is now evident in the form of small droplets of high contact angle ($> 80^{\circ}$) on the surface of the particles. Due to the 3D nature of the bridges and the resolution of the images, an accurate quantification of the contact angles in Figure 8 is not possible. However, it is quite obvious that the menisci are constantly convex. These droplets increase in volume gradually with an increase in R_h and coalesce with neighbouring droplets once they come into sufficiently close proximity [32]. If the adjoining droplets are appended to the same particle, then the smaller of the two will disappear in favour of the larger, since smaller drops have higher inner pressure making them

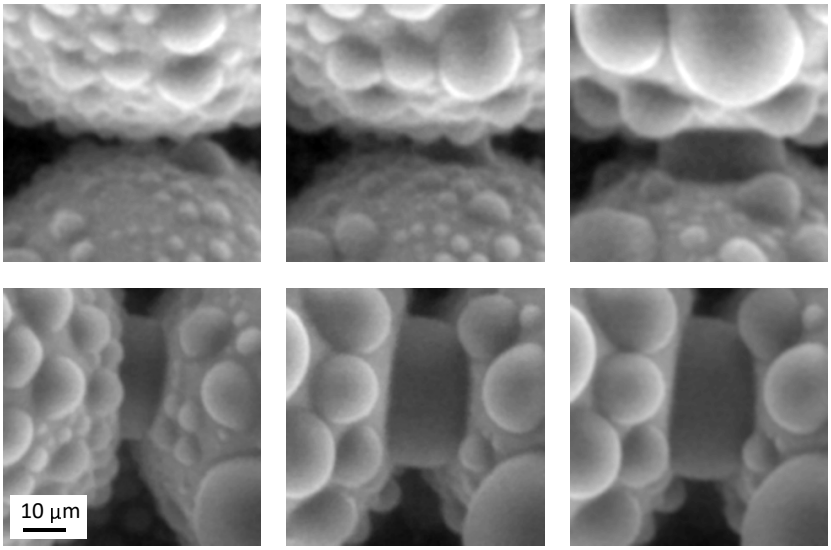

Figure 9: Zoom in liquid bridge evolution in HPB-GB-01 (top row) and HPB-GB-02 (bottom row) during initial wetting phase, from R_h of 98.6 % to 100 %

thermodynamically less stable (water flows to the site of lower pressure). The resulting droplet will adopt the most stable configuration to accommodate the new volume, noting that the triple line may remain pinned if unable to exceed the advancing contact angle (discussed in more detail later in this paper). This is evident by comparing the number and size of droplets on the surfaces of the same particle in subsequent images (e.g. Fig. 8-W5a, W5b; Fig. 9).

Droplets appended to different particles that come into contact coalesce to form a capillary bridge, as it can be seen in the top row of images in Figure 9. By this mechanism, capillary bridges can form between particles at larger separation distances than could be achieved by the same particles with hydrophilic surfaces (see Table 1). The contact angles of the newly formed bridges are initially *smaller* than those of the droplets immediately

prior to coalescence, resulting in a slight attraction of the two particles. Once the volume of the bridge starts to increase so too does the contact angle, and therefore the particles start to move apart (see video submission). Figure 9 also shows that, when the bridge contact angle increases sufficiently, the triple line spreads, keeping the high contact angles relatively constant thereafter.

Similarly to HPL-GB-01 until the end of the initial wetting phase the sample is consistently in the pendular regime, before suddenly flooding (mainly coming from the substrate that has a higher degree of wettability than the particles), reaching a capillary regime when the chamber reaches $R_h = 100\,\%$ (Fig. 8-W5b). Due to the hydrophobic nature of the particles, at R_h of $100\,\%$ we can still detect individual menisci (Fig. 8-W5b top right) and droplets on the exposed tops of the particles, something that did not occur in HPL-GB-01, as these locations are disconnected from the inundating water. In the first desorption phase, large individual condensation droplets form on the tops of the particles. These droplets have a higher image intensity near their edge (i.e. halos), indicating that their surface curves in plane, as shown by [64], confirming the high contact angle (hidden beneath the droplet). Towards the end of the initial drying phase water forming between the particles and the substrate slightly reduces in volume, as do the surface droplets with some evaporating completely. However, the sample seems to remain in a capillary regime, contrary to HPL-GB that reached a lower degree of saturation at D4.

Water repellence allows the surface droplets to reach impressive volumes during the second wetting phase, appearing in width almost as large as the particles themselves (ranging from a few to 85 µm; e.g. Fig. 8-W8). Droplets

increase in volume until contacting and merging with the surrounding continuous water (e.g. Fig. 8-W8 vs W9). Once again, the larger volume of water surrounding the grains makes the droplets (smaller in volume) thermodynamically unstable, explaining why they disappear in favour of the surrounding pool of water.

As found for HPL-GB-01, the final drying phase reveals little difference in the amount of water in the specimen chamber (e.g. Fig. 8-D5 vs D7). This is contrary to the response of the hydrophilic glass beads where there is a clear reduction in the volume of water that occupies the micrographs during the drying stages (e.g. Fig. 6-D5 vs D7). According to Eq. 6 and accepting that the water surrounding the particles (capillary regime) will be curved downwards towards the substrate for HPL-GB-01 and upwards for HPB-GB-01, the vapour pressure above the curved interface is higher in HPB-GB-01 than that for the concave interface of the HPL-GB-01. Specifically, at the interface between the liquid and the surrounding air of a convex liquid surface, the vapor concentration exceeds the saturation value for a free surface, making it therefore harder for water molecules to evaporate, above whatever detrimental effects arise from the presence of the adhesive substrate. We note, however, that the water level in the continuous phase may vary normal to the the plane of the micrograph, which is not discernible in these images if portions of the particles are not exposed. Hysteresis between the wetting and drying behaviour would appear, however, to be less than what was observed for the hydrophilic glass beads. A suitable definition of hysteresis, however, may be difficult to provide as, unlike for the hydrophilic beads, a set of retention curves cannot be drawn for HPB-GB-01 due to the

hydrophobic surfaces.

3.2.2. Sands

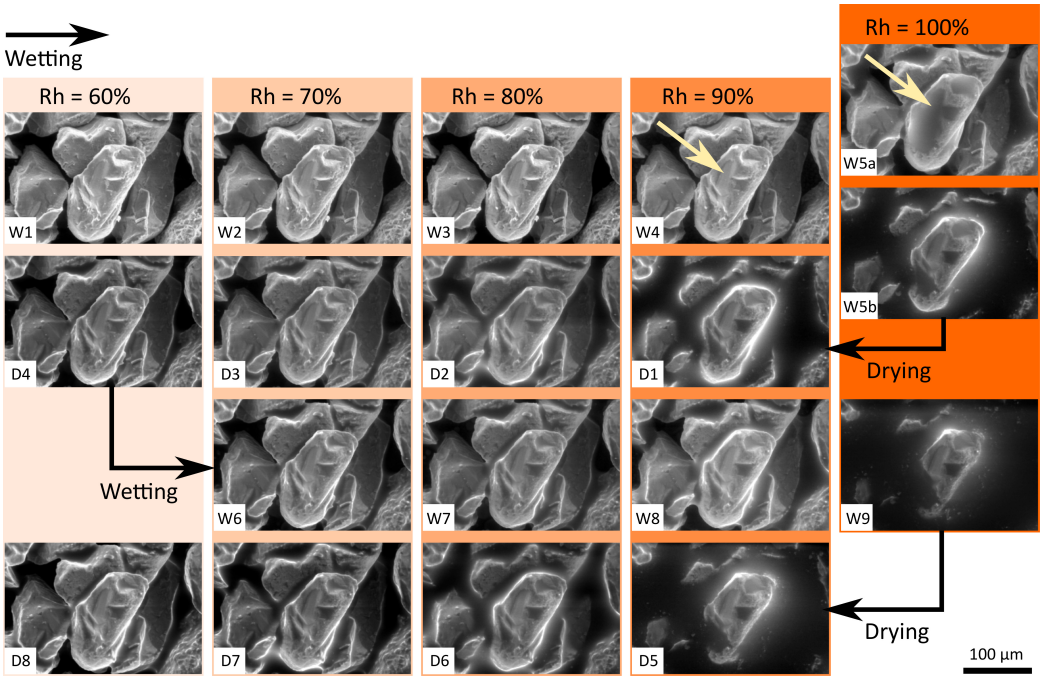

Figure 10: ESEM micrographs showing particles undergoing two full wetting and drying cycles of HPL-S-01

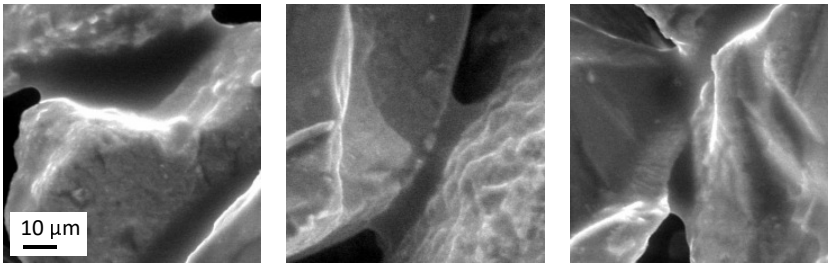

Figure 11: Zoom in concave liquid bridges in HPL-S-01

Figure 10 shows the evolution of menisci structures in HPL-S-01. Note

that, due to the overlapping of the particles, measurements of the separation distances and the solid fraction are not possible. It is not immediately obvious that there is condensation in the first wetting phase as R_h increases. However, the loss of definition of particle surface features and the darkening of concave areas on the particles (Fig. 10-W4 $\rightarrow$ W5a area marked with arrows) signifies the presence of water in the images. Like in HPL-GB-01 some particles appear to be slightly attracted once a bridge forms between them, indicating suction. The few bridges that form between particles are concave, e.g. as shown in the examples in Figure 11, however many bridges are obscured by overhanging sections of particles. Additionally, all visible menisci are both asymmetric and axisymmetric due to the irregular particle shapes; a phenomenon that was not observed in HPL-GB.

During the initial drying stage (Fig. 10-D1$\rightarrow$D4) water gradually recedes and some of the formerly formed bridges reappear. The response of the material is visually similar during the second wetting and drying stages to what is observed in the first. Given that, it seems that hysteresis between wetting and drying is less than what was found for HPL-GB-01; however, it is not possible to evaluate hysteresis quantitatively, or even schematically, as much of the water phase is obscured. Suction hysteresis in natural sands is, however, well understood [e.g. 29].

Figure 12 shows the evolution of meniscus structures in HPB-S-01. Droplets appear on the particle surfaces during the first wetting phase as R_h increases, however these are not as well defined as in HPB-GB-01 due to the surface texture of the sand grains. The first liquid bridges form between neighbouring particles with small separation distances at $R_h = 80\,\%$, again through

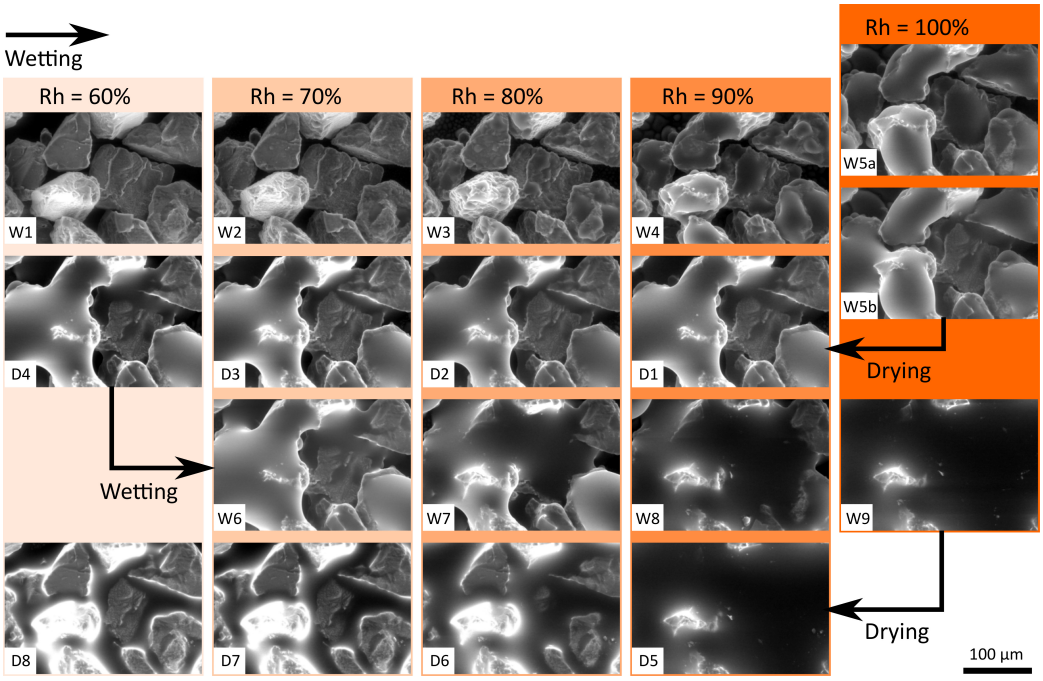

Figure 12: ESEM micrographs showing particles undergoing two full wetting and drying cycles of HPB-S-01

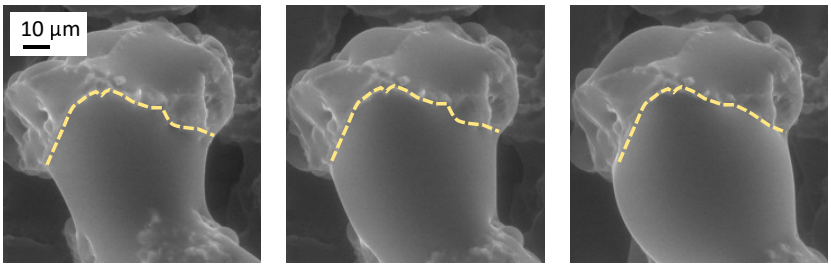

Figure 13: Pinning of the triple line and formation of initially concave asymmetric bridge (left) evolving to an almost cylindrical bridge (middle) to finally forming a convex asymmetric bridge (right) during the initial wetting stage. [Note: The dashed line signifies the triple line].

599 the coalescence of droplets between neighbouring particles as seen in HPB-
600 GB-01. However, the bridges and menisci differ greatly in volume and shape

as the non-spherical nature of the sand particles prevents traditional (axisymmetric) liquid bridges from forming; rather, all of the capillary bridges appear to be asymmetric (Fig. 12-W5a, W5b).

Notably, although most capillary bridges appear to have a high contact angle, they are not all convex (e.g. Fig. 12-W4 bottom left and W5a top right). This is not a case of having mixed hydrophilic and hydrophobic particles, as droplets appearing on the surface of the particles between which concave menisci structures form confirms the hydrophobicity of those surfaces. Rather, the limited volume of water (restrained to that contained within the coalescing droplets, as water cannot displace via adsorbed films) can produce an initially concave bridge if the volume of the two coalescing drops is relatively low, the separation distance large and for a pinned triple line geometry. The volume of the bridge increases with an increase in R_h, however a pinned triple line will result in the bridge gradually becoming convex. This process is highlighted in Figure 13, where an initially concave bridge becomes convex as R_h increases. The hydromechanical response of such an assembly may therefore vary considerably at the moment of bridge formation; an observation which will be explored in future studies.

Unlike for HPB-GB-01, the hydrophobic sand does not reach full saturation at $R_h = 100\,\%$ at the end of the first wetting phase; individual bridges between two particles are still evident. Between Fig. 12-W5b and -D1, however, several bridges coalesce, so that the individual convex bridges in -W5b conjoin to form several concave bridges. Again, the hydromechanical implications of this transition are likely to be complex as particles shift between repulsive and attractive forces. Notably, with further drying there is negli-

gible apparent reduction in the amount of moisture in the sample, whereby the sample remains in a funicular regime. The bridges expand again with the beginning of the second wetting stage (Fig. 12-W6). Between -W6 and -W8, water appears to build up on the rearmost particles, causing the bridges to coalesce and grow into the central region of the image. Unlike for the first wetting stage, the sample has completely flooded by the end of the second wetting stage. In the final drying stage, a small portion of the overall water evaporates, exposing the tops of the particles, however no bridges seem to reappear (Fig. 12-D5 $\rightarrow$ D8), similar to what was seen in HPB-GB-01. Hysteresis is therefore suggested between the second wetting and drying phases; however, again, a quantitative assessment cannot be made as much of the water volume is obscured.

A previous study, [45], suggested that the shape of the menisci are controlled by the nature of the materials and not the size and shape of the individual particles. However, when comparing the response of sand and glass beads it is clear that the shape and surface roughness of the sand particles has contributed to the formation of both asymmetric and interchangeable concave and convex meniscus structures. Despite the degree (or not) of water repellence, the effect of the particle geometry should not be neglected when interpreting hydromechanical responses (e.g. in numerical and constitutive models). Additionally, [8] suggested that the soil physics theory developed for hydrophilic soils is valid for hydrophobic soils provided a correction for the contact angle effect is included. From our analysis we can clearly see that the responses of the materials varied significantly and it was not just a case of exhibiting different meniscus shapes, which would justify a simple

correction of the contact angle to the existing theories. It is noted, however, that the work presented here provides a qualitative description of the water retention characteristics, and that deeper explorations of the exact natures and pressures of the identified meniscus structures are warranted; the work presented here therefore represents the first step towards a physically meaningful hydraulic interpretation of these materials.

4. Conclusions

In this work we investigated experimentally the interaction of water with artificially hydrophobised samples of a natural sand and spherical glass beads in the macro-scale using the sessile drop method and the micro-scale using ESEM micrographs. Understanding the effect of particle shape, liquid volume and hyrdophobicity on the values of the contact angles will provide a basis upon which the hydro-mechanical stability of these assemblies can be explored. The main arguments and findings are summarised below:

1. Goniometer results showed the clear effect of the particle shape on the value of the apparent contact angle, as the hydrophobic sand exhibited consistently lower values than the glass beads and vice versa in the case of the hydrophilic materials. This was contrary to some previous results presented in the literature and is attributed to the higher interlocking of the sand grains, resulting in a less rough surface upon which the sessile drop was deposited.

2. Drop shape analyses indicated increasing apparent contact angles with increasing droplet volumes for both the hydrophilic and hydrophobic

sand grains. This was attributed to the presence of a greater number of sharp or distinct edges of the sand grains interacting with the expanding triple line (i.e. an increasing sessile drop volume), an effect that has previously not been considered, and a simple mathematical model was presented to support the findings.

3. ESEM micrographs showed that the hydrophilic glass beads demonstrated classically understood meniscus formation and growth mechanisms. The hydrophilic sand exhibited a similar retention behaviour to that of the hydrophilic glass beads but with slightly less hysteresis, as menisci were pinned and less able to reform or rupture. Whilst both the hydrophilic glass beads and the sand have a reasonably similar packing, the non-spherical shape of the sand particles resulted in a different pore space geometry to the highly regular one in the glass beads. Hence, both pendular and funicular regimes were observed in the hydrophilic sand, but not the glass beads, before reaching full saturation.

4. In the hydrophobic glass beads, convex bridges were observed to form at particle contacts, as described in classical theory, and between separated neighbouring particles, which has not yet been observed. However, in the hydrophobic sand, coexisting axisymmetric and asymmetric, concave and convex bridges with varying volumes were observed. This was attributed to the pinning mechanism, which prevented the triple line from advancing or receding over irregular hydrophobic surfaces.

5. As larger condensation droplets could be supported on the hydropho-

bic surfaces, bridging was observed to develop over considerably larger (even by tenfold) particle separation distances between hydrophobic particles than between the same particles in a hydrophilic state. At the point of coalescence, a bridge could be concave or convex, depending on the separation distance being spanned, the combined volume of the coalesced droplets and the pinning of the triple line.

6. Evidence has been found (see video submissions) of attractive forces acting between hydrophilic glass beads on the formation of a liquid bridge, supporting classical theory. Whereas, in the case of hydrophobic glass beads, particles may instantaneously *attract* on bridge formation (high contact angle bridge, yet below 90° due to the low volume of the adjoined condensation droplets and the high separation distances). However, subsequent growth of the bridge returns it to a traditionally expected convex shape and the particles are repelled.

Appendix A: Edge model calculations

The coordinates (x_i,y_i) of the intersection points between the circular triple line and a linear edge were calculated using the circle's central coordinate and radius r and the edge's gradient m and y axis intercept.

The interception angle β was defined as the angle between the triple line radius and the edge, as shown in Figure A.1, where:

$$\beta = \cos^{-1}\left(\frac{d}{2r}\right) \tag{A.1}$$

and where d is the distance between the two intersection points,

$$d = \sqrt{(x_2 - x_1)^2 + (y_2 - y_1)^2} \tag{A.2}$$

noting that the quadratic equation was used to replace the subtractive terms in Eq. A.2 to improve numerical stability. For perpendicular intersections, $d = 2r$ and for tangential intersections, $(x_1,y_1) = (x_2,y_2)$.

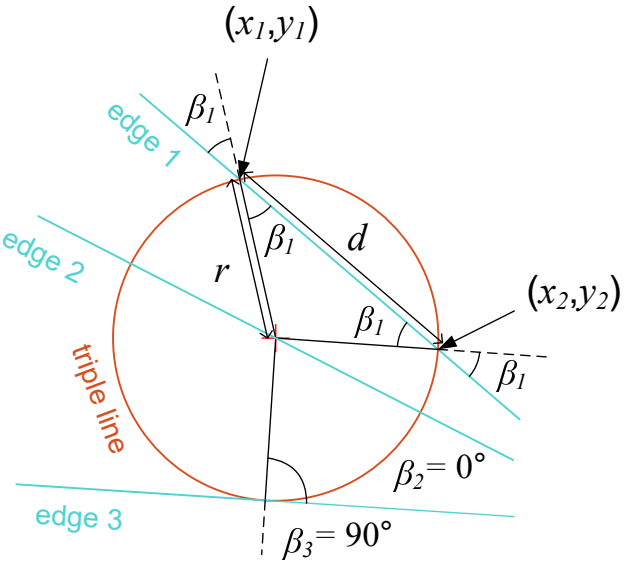

Figure A.1: Calculation of the intersection angle β for triple line intersections with a linear edge, showing an intersection at an arbitrary angle (β_1), a perpendicular intersection (β_2) and a tangential intersection (β_3)

It was assumed that a triple line with a larger radius would be more greatly affected by a linear edge than a triple line of a smaller radius. The cosine of the arc angle ϕ, as defined in Figure A.2, was therefore used to weight the effect of a larger or smaller radius, according to:

$$\phi = \tan^{-1}\left(\frac{a}{r}\right) \tag{A.3}$$

where $\cos\phi$ approaches unity for large radii and is small for small radii. We note that Eq. A.3 is only appropriate for $r >> a$ and that, here, we have $r \approx a$ for some cases. Furthermore, the position of the intersection along a

has not been considered. However, for the purposes of this initial model, we believe that Eq. A.3 is adequate to capture the general effect of an increasing radius on likely edge interaction.

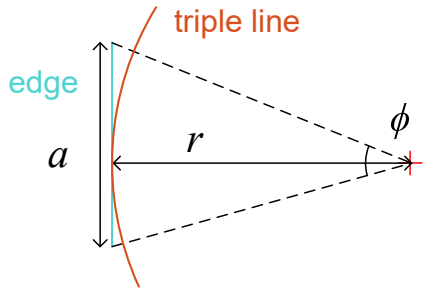

Figure A.2: Calculation of the arc angle ϕ to account for the effect of triple line curvature on edge interaction

Acknowledgements

The RH110 Silica Sand was kindly supplied by Minerals Marketing Ltd. The authors would like to thank the following colleagues at the University of Edinburgh, UK: Mr M. Corcoran for his help inducing hydrophobicity to the soil samples, Ms V. Kubishkina for her help with the goniometer, Mr G. Sim for the particle size analysis and Prof. G. McHale for our fruitful discussions. This work is funded under the EPSRC New Investigator Award EP/S011005/1.

References

[1] Arye, G., Tarchitzky, J., Chen, Y., 2011. Treated wastewater effects on water repellency and soil hydraulic properties of soil aquifer treatment infiltration basins. Journal of Hydrology 397, 136 – 145.

[2] Bachmann, J., Arye, G., Deurer, M., Woche, S., Horton, R., Hartge, K.H., Chen, Y., 2006. Universality of a surface tension—contact-angle relation for hydrophobic soils of different texture. Journal of Plant Nutrition and Soil Science 169, 745 – 753.

[3] Bachmann, J., Ellies, A., Hartge, K., 2000a. Development and application of a new sessile drop contact angle method to assess soil water repellency. Journal of Hydrology 231-232, 66 – 75.

[4] Bachmann, J., Horton, R., van der Ploeg, R.R., Woche, S., 2000b. Modified sessile drop method for assessing initial soil–water contact angle of sandy soil. Soil Science Society of America Journal 64, 564 – 567.

[5] Bachmann, J., Woche, S.K., Goebel, M.O., Kirkham, M.B., Horton, R., 2003. Extended methodology for determining wetting properties of porous media. Water Resources Research 39.

[6] Bardet, J., Jesmani, M., Jabbari, N., 2011. Effects of compaction on shear strength of wax-coated sandy soils. Electronic Journal of Geotechnical Engineering 16 D, 451 – 461.

[7] Bardet, J.P., Jesmani, M., Jabbari, N., 2014. Permeability and compressibility of wax-coated sands. Géotechnique 64, 341 – 350.

[8] Bauters, T., Steenhuis, T., DiCarlo, D., Nieber, J., Dekker, L., Ritsema, C., Parlange, J.Y., Haverkamp, R., 2000. Physics of water repellent soils. Journal of Hydrology 231-232, 233 – 243.

[9] Bauters, T.W.J., Steenhuis, T.S., Parlange, J.Y., DiCarlo, D.A., 1998.

759 Preferential flow in water-repellent sands. Soil Science Society of Amer-
760 ica Journal 62, 1185 – 1190.

761 [10] Beckett, C., Fourie, A., Toll, D., 2016a. Water repellent soils: the case
762 for unsaturated soil mechanics.

763 [11] Beckett, C.T.S., Augarde, C.E., 2013. Prediction of soil water retention
764 properties using pore-size distribution and porosity. Canadian Geotech-
765 nical Journal 50, 435 – 450.

766 [12] Beckett, C.T.S., Fourie, A.B., Toll, D.G., 2016b. Water repellent soils:
767 The case for unsaturated soil mechanics, in: Proceedings of the 3rd
768 European Conference on Unsaturated Soils - "E-UNSAT 2016".

769 [13] Camenen, J.F.m.c., Descantes, Y., 2017. Geometrical properties of rigid
770 frictionless granular packings as a function of particle size and shape.
771 Phys. Rev. E 96, 012904. URL: https://link.aps.org/doi/10.1103/
772 PhysRevE.96.012904, doi:10.1103/PhysRevE.96.012904.

773 [14] Cassie, A.B.D., Baxter, S., 1944. Wettability of porous surfaces. Trans.
774 Faraday Soc. 40, 546 – 551.

775 [15] Czachor, H., Doerr, S., Lichner, L., 2010. Water retention of repellent
776 and subcritical repellent soils: New insights from model and experimen-
777 tal investigations. Journal of Hydrology 380, 104 – 111.

778 [16] Danilatos, G.D., 1993. Introduction to the ESEM instrument. Mi-
779 croscopy Research and Technique 25, 354 – 361.

[17] DeBano, L., 2000. The role of fire and soil heating on water repellency in wildland environments: a review. Journal of Hydrology 231-232, 195 – 206.

[18] Dekker, L.W., Jungerius, P.D., 1990. Water repellency in the dunes with special reference to the netherlands. Catena, Supplement , 173 – 183.

[19] Doerr, S.H., Shakesby, R.A., Walsh, R.P.D., 2000. Soil water repellency: its causes, characteristics and hydro-geomorphological significance. Earth-Science Reviews 51, 33 – 65.

[20] Dörmann, M., Schmid, H.J., 2017. Distance-dependency of capillary bridges in thermodynamic equilibrium. Powder Technology 312, 175 – 183. doi:https://doi.org/10.1016/j.powtec.2017.01.012.

[21] Emerson, W., Bond, R.D., 1963. The rate of water entry into dry sand and calculation of the advancing contact angle. Soil Research 1 , 9 – 16.

[22] Eral, H., 't Mannetje, D.J.C.M., Oh, J., 2013. Contact angle hysteresis: a review of fundamentals and applications. Colloid and Polymer Science 291, 247 – 260.

[23] Farmer, T.P., Bird, J.C., 2015. Asymmetric capillary bridges between contacting spheres. Journal of Colloid and Interface Science 454, 192 – 199.

[24] Gagneux, G., Millet, O., 2014. Analytic calculation of capillary bridge properties deduced as an inverse problem from experimental data. Transport in Porous Media 105, 117 – 139.

[25] Gao, L., McCarthy, T.J., 2006. Contact angle hysteresis explained. Langmuir 22, 6234 – 6237.

[26] de Gennes, P.G., Brochard-Wyart, F., Quéré, D., 2004a. Capillarity: Deformable Interfaces. Springer New York, New York, NY. pp. 1 – 31.

[27] de Gennes, P.G., Brochard-Wyart, F., Quéré, D., 2004b. Special Interfaces. Springer New York, New York, NY. pp. 215 – 259.

[28] Gens, A., 2010. Soil-environment interactions in geotechnical engineering. Géotechnique 60, 3–74.

[29] Haines, W.B., 1930. Studies in the physical properties of soil. V. The hysteresis effect in capillary properties, and the modes of moisture distribution associated therewith. The Journal of Agricultural Science 20, 97 – 116.

[30] Han, T.Y., Shr, J.F., Wu, C.F., Hsieh, C.T., 2007. A modified wenzel model for hydrophobic behavior of nanostructured surfaces. Thin Solid Films 515, 4666 – 4669.

[31] Hensel, R., 2014. Robust omniphobic surfaces by mimicking the springtail skin morphology. Ph.D. thesis. Technischen Universität Dresden.

[32] Iwamatsu, M., Horii, K., 1996. Capillary condensation and adhesion of two wetted surfaces. Journal of Colloid and Interface Science 182, 400 – 406.

[33] Kang, H., Lourenço, S.D.N., Yan, R., 2019. Droplet interaction with hydrophobic granular materials: An insight with the lattice boltzmann

method, in: Zhan, L., Chen, Y., Bouazza, A. (Eds.), Proceedings of the 8th International Congress on Environmental Geotechnics Volume 3, Springer Singapore, Singapore. pp. 219 – 226.

[34] Karatza, Z., Buckman, J., Medero, G.M., Beckett, C.T.S., 2020. Effect of wetting and drying on meniscus structures in hydrophobic sands. E3S Web Conf. 195, 03040.

[35] Karim, M.Z., Tucker-Kulesza, S.E., Derby, M.M., 2018. Synthesizing hydrophobic sand and comparison of shear strength properties with hydrophilic sand, in: IFCEE 2018, pp. 75 – 83.

[36] Kasangaki, G., 2012. Experimental study of hydro-mechanical behaviour of granular materials. Ph.D. thesis. Heriot-Watt University, UK.

[37] King, P., 1981. Comparison of methods for measuring severity of water repellence of sandy soils and assessment of some factors that affect its measurement. Soil Research 19, 275 – 285.

[38] Kirkham, M., 2014. Chapter 4 - soil–water terminology and applications, in: Kirkham, M. (Ed.), Principles of Soil and Plant Water Relations (Second Edition). second edition ed.. Academic Press, Boston, pp. 41 – 52.

[39] Krüss GmbH, 2014-2016. ADVANCE for Drop Shape Analyzers - User Manual. Krüss GmbH. Borsteler Chaussee 85, 22453 Hamburg, Germany.

[40] Leelamanie, D.A.L., Karube, J., 2009. Time dependence of contact angle

and its relation to repellency persistence in hydrophobized sand. Soil Science & Plant Nutrition 55, 457 – 461.

[41] Leelamanie, D.A.L., Karube, J., Yoshida, A., 2008. Characterizing water repellency indices: Contact angle and water drop penetration time of hydrophobized sand. Soil Science & Plant Nutrition 54, 179 – 187.

[42] Leong, E.C., Rahardjo, H., 1997. Review of soil-water characteristic curve equations. Journal of Geotechnical and Geoenvironmental Engineering 123, 1106 – 1117.

[43] Lin, H., Lourenço, S.D., 2020. Physical degradation of hydrophobized sands. Powder Technology 367, 740 – 750.

[44] Liu, H., Ju, Z., Bachmann, J., Horton, R., Ren, T., 2012. Moisture-dependent wettability of artificial hydrophobic soils and its relevance for soil water desorption curves. Soil Sci. Soc. Am. J. 76, 342 – 349.

[45] Lourenço, S., Gallipoli, D., Augarde, C., Toll, D., Fisher, P., Congreve, A., 2012. Formation and evolution of water menisci in unsaturated granular media. Géotechnique 62, 193 – 199.

[46] Lourenço, S.D.N., Woche, S.K., Bachmann, J., Saulick, Y., 2015. Wettability of crushed air-dried minerals. Géotechnique Letters 5, 173 – 177.

[47] Mao, J., Nierop, K., Dekker, S., Dekker, L., Chen, B., 2019. Understanding the mechanisms of soil water repellency from nanoscale to ecosystem scale: a review. J Soils Sediments 19, 171 – 185.

[48] Ma'shum, M., Farmer, V., 1985. Origin and assessment of water repellency of a sandy south australian soil. Soil Research 23, 623 – 626.

[49] Ma'shum, M., Tate, M.E., Jones, G.P., Oades, J.M., 1988. Extraction and characterization of water–repellent materials from australian soils. Journal of Soil Science 39, 99 – 110.

[50] McCerery, R., Woodward, J., McHale, G., Winter, K., Armstrong, S., Orme, B.V., 2021. Slippery liquid-infused porous surfaces: The effect of oil on the water repellence of hydrophobic and superhydrophobic soils. European Journal of Soil Science 72, 963 – 978.

[51] McHale, G., 2007. Cassie and wenzel: were they really so wrong? Langmuir 23, 8200 – 8205.

[52] Molenkamp, F., Nazemi, A.H., 2003. Interactions between two rough spheres, water bridge and water vapour. Géotechnique 53, 255 – 264.

[53] Mu, F., Su, X., 2007. Analysis of liquid bridge between spherical particles. China Particuology 5, 420 – 424.

[54] Nazemi, A., Majnooni-Heris, A., 2012. A mathematical model for the interactions between non-identical rough spheres, liquid bridge and liquid vapor. Journal of Colloid and Interface Science 369, 402 – 410.

[55] Ng, C.W., Pang, Y.W., 2000. Experimental investigations of the soil-water characteristics of a volcanic soil. Canadian Geotechnical Journal 37, 1252 – 1264.

[56] Ng, S.H.Y., Lourenço, S.D.N., 2016. Conditions to induce water repellency in soils with dimethyldichlorosilane. Géotechnique 66, 441 – 444.

[57] Nguyen, H.N.G., Millet, O., Gagneux, G., 2019. On the capillary bridge between spherical particles of unequal size: analytical and experimental approaches. Continuum Mechanics and Thermodynamics 31, 225 – 237.

[58] Noll, W., 1968. CHAPTER 3 - Monomeric Organosilicon Compounds RnSiX4–n, in: Chemistry and Technology of Silicones. Academic Press, pp. 67 – 123.

[59] Oliver, J.F., Huh, C., Mason, S.G., 1977. Resistance to spreading of liquids by sharp edges. Journal of Colloid and Interface Science 59, 568–581. doi:10.1016/0021-9797(77)90052-2.

[60] Payam, A.F., Fathipour, M., 2011. A capillary force model for interactions between two spheres. Particuology 9, 381 – 386. Multiscale Modeling and Simulation of Complex Particulate Systems.

[61] Saulick, Y., Lourenço, S., Baudet, B., 2017. A semi-Automated technique for repeatable and reproducible contact angle measurements in granular materials using the sessile drop method. Soil Science Society of America Journal 81, 241 – 249.

[62] Schindelin, J., Arganda-Carreras, I., Frise, E., 2012. Fiji: an open-source platform for biological-image analysis. Nature methods 9, 676 – 682.

[63] Shakesby, R., Doerr, S., Walsh, R., 2000. The erosional impact of soil

hydrophobicity: current problems and future research directions. Journal of Hydrology 231-232, 178 – 191.

[64] Stelmashenko, N.A., Craven, J.P., Donald, A.M., Terentjev, E.M., Thiel, B.L., 2001. Topographic contrast of partially wetting water droplets in environmental scanning electron microscopy. Journal of Microscopy 204, 172 – 183.

[65] Subedi, S., Kawamoto, K., Jayarathna, L., Vithanage, M., Moldrup, P., Wollesen de Jonge, L., Komatsu, T., 2012. Characterizing time-dependent contact angles for sands hydrophobized with oleic and stearic acids. Vadose Zone Journal 11.

[66] Tarantino, A., 2013. Basic Concepts in the Mechanics and Hydraulics of Unsaturated Geomaterials. John Wiley & Sons, Ltd. chapter 1. pp. 1 – 28.

[67] Tarchitzky, J., Lerner, O., Shani, U., Arye, G., Lowengart-Aycicegi, A., Brener, A., Chen, Y., 2007. Water distribution pattern in treated wastewater irrigated soils: hydrophobicity effect. European Journal of Soil Science 58, 573 – 588.

[68] Tuller, M., Or, D., 2005. Water retention and characteristic curve, in: Hillel, D. (Ed.), Encyclopedia of Soils in the Environment. Elsevier, Oxford, pp. 278 – 289.

[69] Valsamis, J.B., Volder, M.D., Lambert, P., 2013. Physical Background. Springer Berlin Heidelberg, Berlin, Heidelberg. pp. 3 – 16.

933 [70] Wallis, M., Horne, D., 1992. Soil water repellency, in: Stewart, B. (Ed.),
934 Advances in Soil Science. Springer, New York, NY. volume 20.

935 [71] Wenzel, R.N., 1936. Resistance of solid surfaces to wetting by water.
936 Industrial & Engineering Chemistry 28, 988 – 994.

937 [72] Wijewardana, N., Kawamoto, K., Moldrup, P., Komatsu, T., Kuruku-
938 lasuriya, L., Priyankara, N., 2015. Characterization of water repellency
939 for hydrophobized grains with different geometries and sizes. Environ
940 Earth Sci 74, 5525 – 5539.

941 [73] Wijewardana, N.S., Müller, K., Moldrup, P., Clothier, B., Komatsu,
942 T., Hiradate, S., de Jonge, L.W., Kawamoto, K., 2016. Soil-water repel-
943 lency characteristic curves for soil profiles with organic carbon gradients.
944 Geoderma 264, 150 – 159.

945 [74] Zheng, S., Lourenço, S.D.N., Cleall, P.J., Millis, S.W., Ng, A.K.Y., Chui,
946 T.F.M., 2017. Synthetic water repellent soils for slope stabilization, in:
947 Mikoš, M., Arbanas, Ž., Yin, Y., Sassa, K. (Eds.), Advancing Culture
948 of Living with Landslides, Springer International Publishing, Cham. pp.
949 523 – 528.

950 [75] Zhou, Z., Leung, A.K., Zhu, W.J., Li, Y.Y., 2021. Hydromechanical
951 behavior of unsaturated artificially–hydrophobized sand: Compression,
952 shearing, and dilatancy. Engineering Geology 291, 106223.